

A finite-difference scheme for three-dimensional incompressible flows in spherical coordinates

L. Santelli¹, P. Orlandi² & R. Verzicco^{1,3,4}

¹ *Gran Sasso Science Institute, L'Aquila, Italy*

² *Sapienza Università di Roma, Roma, Italy*

³ *Università di Roma 'Tor Vergata', Roma, Italy*

⁴ *PoF, University of Twente, Enschede, The Netherlands*

Abstract

In this study we have developed a flexible and efficient numerical scheme for the simulation of three-dimensional incompressible flows in spherical coordinates. The main idea, inspired by a similar strategy as [1] for cylindrical coordinates, consists of a change of variables combined with a discretization on a staggered mesh and the special treatment of few discrete terms that remove the singularities of the Navier–Stokes equations at the sphere centre and along the polar axis. This new method alleviates also the time step restrictions introduced by the discretization around the polar axis while the sphere centre still yields strong limitations, although only in very unfavourable flow configurations.

The scheme is second-order accurate in space and is verified and validated by computing numerical examples that are compared with similar results produced by other codes or available from the literature.

The method can cope with flows evolving in the whole sphere, in a spherical shell and in a sector without any change and, thanks to the flexibility of finite-differences, it can employ generic mesh stretching (in two of the three directions) and complex boundary conditions.

Keywords:

Thanks to the growing availability of computational power also the complexity of flows tackled by numerical simulations is increasing. Among many, one of the challenges of a computation is the mathematical description of non trivial domains and the flows developing within spherical geometries belong to this category.

Indeed, the mapping of spherical to Cartesian coordinates reads $x = r \cos \theta \sin \phi$, $y = r \sin \theta \sin \phi$, $z = r \cos \phi$, (Fig. 1) and it is not single valued at the centre ($r = 0$) and on the polar axis ($\phi = 0, \pi$) therefore, even if the sphere is among the simplest shapes, its natural coordinate system contains mathematical singularities that are reflected also in the governing equations for fluid flows (see next section).

Spherical domains have been traditionally used in geophysics [2], oceanography [3], meteorology [4], astrophysics [5], [6] and magnetohydrodynamics [7] although they are gaining popularity also for industrial [8] and fundamental problems [9], [10], [11].

In fact, an important advantage of the spherical coordinates is that their highest degree of symmetry imposes no preferred orientation and this is a desired property when the system evolves in an unbounded space [12]. That the mesh topology could interfere with the flow dynamics was shown by [1] who computed the evolution of an azimuthally unstable toroidal vortex ring on a Cartesian square mesh and obtained preferentially the $n = 4$ wavenumber even if the linear stability analysis predicted the $n = 5$ mode. On the other hand, the same phenomenon, simulated using a polar cylindrical mesh [13], correctly showed the emergence of fivefold symmetric structures as expected from the theory [14].

Since the early stability analyses of thermal convection in spherical shells [9], also in later studies [6], [15], [16], [17] the variables were expressed by spherical harmonics for the longitude θ and colatitude ϕ while Chebyshev polynomials were mostly used for the radial direction r (Fig. 1). This expansion allowed the development of accurate pseudo-spectral methods that avoided the equation singularity at the polar axis.

All these studies, however, did not cope with the singularity at the sphere centre ($r = 0$) since the equations were solved only in the gap between two concentric spheres.

On the other hand, [18] developed a spectral method that could discretize the equations up to the sphere centre by using only the even order Chebyshev polynomials for the radial direction that avoided the unnecessary mesh refinement near the origin. Also [19] simulated the whole sphere although they used Jacoby polynomials that, in addition to the previous property, satisfy also the regularity conditions at the poles. Using this numerical scheme [20] were able to simulate magnetohydrodynamic processes in a precessing sphere. [21] developed a Navier–Stokes spectral solver in a sphere employing a latitude dependent number of modes that avoided the difficulties with the

sphere centre and polar axis.

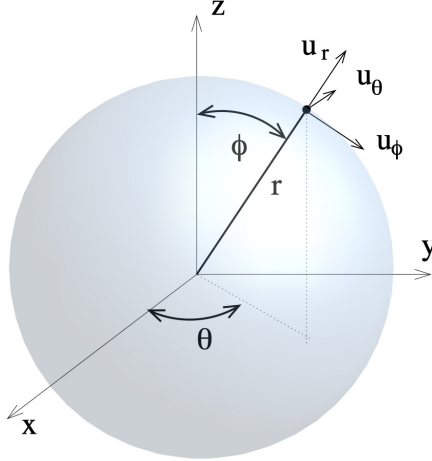


Figure 1: Sketch of the system and coordinate definition.

Spectral methods are generally preferred to other approaches since, although the overall accuracy depends also on the dealiasing schemes, they yield smaller numerical errors for a given number of nodes (modes). However, as shown by [22], finite-difference approximations, if properly implemented, become very competitive cost-wise with respect to spectral methods even considering that the former require more computational nodes to achieve the same precision. In addition, if the simulation has to cope with complex boundary conditions, variable fluid properties or generic node distributions then finite-differences are the best option.

Despite these advantages, the literature on finite-difference methods for the solution of the Navier-Stokes equations in spherical coordinates is scarce and, to the knowledge of the authors only few studies are available. [23] presented a method for solving the equations in a spherical shell by finite-difference approximations on a staggered mesh in all three directions; the variables were modified at the poles by semi-analytic corrections to avoid stability issues. [24] solved the linear Boussinesq convection in a spherical shell using Fourier modes along the latitude θ and finite-differences in r and ϕ . The model was completed with the nonlinear convective terms in [25] and, in both cases, in order to avoid the stability limitations at the polar axis, a low-pass filtering of the solution was applied around the poles. Apparently,

this smoothing strategy was widely adopted in the atmospheric community and [26] described it in a systematic way.

[27] relied on finite-difference approximations in all three directions for the simulation of convection in a rotating spherical shell and, also in this case, a low-pass filter near the poles was employed.

[28] used the code PARODY to simulate convection-driven numerical dynamos in a spherical shell; in this case second-order finite differences were used only for the radial directions while spherical harmonics were adopted for the lateral ones. The scheme was very similar to that of [6] although the new radial discretization made the code suitable for parallel computation on distributed memory clusters.

In the paper [29], second-order finite-differences are employed to solve the Navier-Stokes equations in spherical coordinates relying only on the semi-conservative form of the equations and on the discretization on a staggered-mesh to remove the singularities. However, only flows within two spherical shells are considered, thus never coping with the singularity at $r=0$. In addition, all their examples had vanishing meridional velocity at the poles therefore the singularities of the equations were not really tackled.

[30] proposed a clever procedure to avoid the polar singularity (both, cylindrical and spherical) by extending the radial coordinate to negative values and discretizing the domain so that no nodes are located at $r = 0$. They consider the compressible Navier-Stokes equations and use a co-located discretization with high order finite-differences for the radial direction and spectral methods in the remaining ones. The application of the same method to a fully staggered discretization for the incompressible Navier-Stokes equations is not obvious and it would presumably require substantial changes.

The study by [31] uses a finite-volume method to solve the Navier-Stokes equations in spherical coordinates. In this case, however, neither the singularity at the centre nor at the polar axis is encountered since the domain of interest is restricted to a spherical sector in which the self-similar region of a round jet is computed.

In this paper we present a novel numerical method for the solution of the incompressible Navier-Stokes equations in spherical coordinates. It is based on second-order finite-difference approximations on a staggered mesh that, combined with a change of variables and a special treatment of some discretized terms, eliminates the singularities at the polar axis and at the sphere centre, simultaneously. The same method can be applied both, to flows developing in a spherical shell and in the whole sphere up to $r = 0$

without any change in the numerical procedure.

The time step restrictions introduced by the discretization around the polar axis and sphere centre are attenuated for the former region while the latter still gives strong time step limitations, although only in very unfavourable cases with the largest flow velocity occurring at $r = 0$.

We show that the method maintains the second-order accuracy and yields free-divergence velocity fields to machine precision even when using computational meshes that are unnecessarily refined at the polar axis and sphere centre.

The method is verified and validated by computing numerical examples that stress the treatment of the equations at the singular points and by comparing the results with analogous computations available from the literature.

Finally, since the proposed method takes after the scheme of [1] it shares the same variable arrangement and memory layout, therefore it is efficiently and massively parallelized as done in [32].

The paper is organized as follows: in the next section we present the equations and the change of variables adopted to remove the singularity. In section 2 we discuss the discretization of the variables and the technicalities needed for some terms while in section 3 we briefly describe the numerical method. In section 4 a number of numerical examples is shown and discussed to assess the reliability and efficiency of the method. Finally in section 5 the closing remarks and perspectives for future work are given.

1. The equations

The continuity and momentum equations for an incompressible and viscous flow, in non dimensional form and in spherical coordinates, read [33]:

$$\begin{aligned} \frac{1}{r^2} \frac{\partial r^2 u_r}{\partial r} + \frac{1}{r \sin \phi} \frac{\partial u_\theta}{\partial \theta} + \frac{1}{r \sin \phi} \frac{\partial \sin \phi u_\phi}{\partial \phi} &= 0, \\ \frac{\partial u_r}{\partial t} + \mathbf{u} \cdot \nabla u_r - \frac{u_\phi^2}{r} - \frac{u_\theta^2}{r} &= -\frac{\partial p}{\partial r} + f_r + \\ \frac{1}{Re} \left(\nabla^2 u_r - \frac{2u_r}{r^2} - \frac{2}{r^2 \sin \phi} \frac{\partial u_\phi \sin \phi}{\partial \phi} - \frac{2}{r^2 \sin^2 \phi} \frac{\partial u_\theta}{\partial \theta} \right), \\ \frac{\partial u_\theta}{\partial t} + \mathbf{u} \cdot \nabla u_\theta + \frac{u_\theta u_r}{r} + \frac{u_\theta u_\phi}{r \tan \phi} &= -\frac{1}{r \sin \phi} \frac{\partial p}{\partial \theta} + f_\theta \end{aligned} \tag{1}$$

$$\begin{aligned}
& + \frac{1}{Re} \left(\nabla^2 u_\theta + \frac{2}{r^2 \sin^2 \phi} \frac{\partial u_r}{\partial \theta} + \frac{2 \cos \phi}{r^2 \sin^2 \phi} \frac{\partial u_\phi}{\partial \theta} - \frac{u_\theta}{r^2 \sin^2 \phi} \right), \\
& \frac{\partial u_\phi}{\partial t} + \mathbf{u} \cdot \nabla u_\phi + \frac{u_\phi u_r}{r} - \frac{u_\theta^2}{r \tan \phi} = -\frac{1}{r} \frac{\partial p}{\partial \phi} + f_\phi \\
& + \frac{1}{Re} \left(\nabla^2 u_\phi + \frac{2}{r^2} \frac{\partial u_r}{\partial \phi} - \frac{u_\phi}{r^2 \sin^2 \phi} - \frac{2 \cos \phi}{r^2 \sin^2 \phi} \frac{\partial u_\theta}{\partial \theta} \right), \tag{2}
\end{aligned}$$

where u_θ , u_r and u_ϕ are the velocity components in the longitudinal, radial and colatitude directions, respectively, p the pressure and f_θ , f_r and f_ϕ forcings that could be used for volume forcings such as Coriolis accelerations. $Re = UL/\nu$ is the Reynolds number defined by appropriate velocity U and length L scales and ν is the kinematic viscosity of the fluid.

In the above equations the following relations are used:

$$\mathbf{u} \cdot \nabla q \equiv u_r \frac{\partial q}{\partial r} + \frac{u_\theta}{r \sin \phi} \frac{\partial q}{\partial \theta} + \frac{u_\phi}{r} \frac{\partial q}{\partial \phi}$$

and

$$\nabla^2 q \equiv \frac{1}{r^2} \frac{\partial}{\partial r} r^2 \frac{\partial q}{\partial r} + \frac{1}{r^2 \sin \phi} \frac{\partial}{\partial \phi} \sin \phi \frac{\partial q}{\partial \phi} + \frac{1}{r^2 \sin^2 \phi} \frac{\partial^2 q}{\partial \theta^2}.$$

As anticipated in the Introduction, many terms of Equations (1–2) become singular at the origin ($r = 0$) and at the North and South poles, respectively, $\phi = 0$ and $\phi = \pi$ (hereinafter referred to as ‘polar axis’) and this is not due to the physics described by the equations but to the spherical coordinate transformation that is not single valued at those points. Another drawback is that the coordinates $r = 0$ and $\phi = 0, \pi$ do not coincide with physical boundaries, such as a solid wall or a slip surface, therefore boundary conditions for the unknowns can not be easily computed there. The same argument does not apply to the longitudes $\theta = 0, 2\pi$ that, being the same physical point, can benefit from periodic boundary conditions that do not need explicit values for the unknowns.

Following [1] and motivated by the above arguments, we introduce a new set of unknowns $\mathbf{q} = (q_\theta, q_r, q_\phi) = (u_\theta, u_r r^2, u_\phi \sin \phi)$ that, according to Equation (1), can also be thought of as volume fluxes. An immediate advantage is that these variables yield $q_r(\theta, 0, \phi) = q_\phi(\theta, r, 0) = q_\phi(\theta, r, \pi) \equiv 0$ therefore transforming the difficult singular points for \mathbf{u} in trivial boundary conditions for \mathbf{q} .

By proper manipulation of Equations (1–2) they can be easily rewritten in terms of the new variables \mathbf{q} :

$$\sin \phi \frac{\partial q_r}{\partial r} + r \frac{\partial q_\theta}{\partial \theta} + r \frac{\partial q_\phi}{\partial \phi} = 0, \quad (3)$$

$$\begin{aligned} \frac{\partial q_\theta}{\partial t} + \frac{1}{r^2} \frac{\partial q_r q_\theta}{\partial r} + \frac{1}{r \sin \phi} \frac{\partial q_\theta^2}{\partial \theta} + \frac{1}{r \sin \phi} \frac{\partial q_\theta q_\phi}{\partial \phi} + \frac{q_\theta q_r}{r^3} + \frac{q_\theta q_\phi}{r \tan \phi \sin \phi} = -\frac{1}{r \sin \phi} \frac{\partial p}{\partial \theta} + f_\theta \\ + \frac{1}{Re} \left(\frac{1}{r^2} \frac{\partial}{\partial r} r^2 \frac{\partial q_\theta}{\partial r} + \frac{1}{r^2 \sin \phi} \frac{\partial}{\partial \phi} \sin \phi \frac{\partial q_\theta}{\partial \phi} + \frac{1}{r^2 \sin^2 \phi} \frac{\partial^2 q_\theta}{\partial \theta^2} \right. \\ \left. + \frac{2}{r^4 \sin \phi} \frac{\partial q_r}{\partial \theta} + \frac{2 \cos \phi}{r^2 \sin^3 \phi} \frac{\partial q_\phi}{\partial \theta} - \frac{q_\theta}{r^2 \sin^2 \phi} \right), \end{aligned} \quad (4a)$$

$$\begin{aligned} \frac{\partial q_r}{\partial t} + \frac{\partial}{\partial r} \left(q_r \frac{q_r}{r^2} \right) + \frac{1}{r \sin \phi} \frac{\partial q_r q_\theta}{\partial \theta} + \frac{1}{r \sin \phi} \frac{\partial q_r q_\phi}{\partial \phi} - \frac{r q_\phi^2}{\sin^2 \phi} - r q_\theta^2 = -r^2 \frac{\partial p}{\partial r} + r^2 f_r \\ \frac{1}{Re} \left(\frac{\partial}{\partial r} r^2 \frac{\partial q_r / r^2}{\partial r} + \frac{1}{r^2 \sin \phi} \frac{\partial}{\partial \phi} \sin \phi \frac{\partial q_r}{\partial \phi} + \frac{1}{r^2 \sin^2 \phi} \frac{\partial^2 q_r}{\partial \theta^2} \right. \\ \left. - \frac{2 q_r}{r^2} - \frac{2}{\sin \phi} \frac{\partial q_\phi}{\partial \phi} - \frac{2}{\sin \phi} \frac{\partial q_\theta}{\partial \theta} \right), \end{aligned} \quad (4b)$$

$$\begin{aligned} \frac{\partial q_\phi}{\partial t} + \frac{1}{r^2} \frac{\partial q_r q_\phi}{\partial r} + \frac{1}{r \sin \phi} \frac{\partial q_\theta q_\phi}{\partial \theta} + \frac{1}{r} \frac{\partial}{\partial \phi} \left(q_\phi \frac{q_\phi}{\sin \phi} \right) + \frac{q_\phi q_r}{r^3} - \frac{q_\theta^2 \cos \phi}{r} = -\frac{\sin \phi}{r} \frac{\partial p}{\partial \phi} + \sin \phi f_\phi \\ + \frac{1}{Re} \left(\frac{1}{r^2} \frac{\partial}{\partial r} r^2 \frac{\partial q_\phi}{\partial r} + \frac{1}{r^2} \frac{\partial}{\partial \phi} \sin \phi \frac{\partial q_\phi / \sin \phi}{\partial \phi} + \frac{1}{r^2 \sin^2 \phi} \frac{\partial^2 q_\phi}{\partial \theta^2} \right. \\ \left. + \frac{2 \sin \phi}{r^2} \frac{\partial q_r / r^2}{\partial \phi} - \frac{q_\phi}{r^2 \sin^2 \phi} - \frac{2 \cos \phi}{r^2 \sin \phi} \frac{\partial q_\theta}{\partial \theta} \right), \end{aligned} \quad (4c)$$

that now can be discretized on a computational grid.

It is worthwhile noticing that the above equations, once discretized on a staggered-mesh, are equivalent to those for the contravariant velocity components (multiplied by the cell volume) in general curvilinear coordinates as shown in [34]. However, the equations in general curvilinear coordinates

entail several metric terms that add to the operation count and to the storage requirement, leaving aside the augmented data-transfer across nodes in parallel computing. On the other hand, in spherical coordinates the metric terms reduce to a one-dimensional vector for the radial direction and a two-dimensional array (obtained by the product of two one-dimensional vectors) for the azimuthal direction [33] thus largely reducing the mentioned drawbacks.

2. Variable discretization

Equations (3, 4a–4c) are discretized by central second-order accurate finite-difference approximations along the same line as [1]. Here we describe the technicalities needed for the calculation of some representative terms.

We refer to the sketch of Fig. 2 where the staggered arrangement of [35] is adopted and the node indices $1 \leq i \leq N_i$, $1 \leq j \leq N_j$, $1 \leq k \leq N_k$ span the $0 \leq \theta \leq 2\pi$, $0 \leq r \leq R$ and $0 \leq \phi \leq \pi$ coordinates, respectively.

Let the nodes **A** and **B** have, respectively, i, j, k and $i + 1, j + 1, k + 1$ indices then $q_r(i, j, k)$ is located at the position $(\theta_{i+1/2}, r_j, \phi_{k+1/2})$ which is the centre of the r -normal face of the cell. Similarly $q_\theta(i, j, k)$ is at $(\theta_i, r_{j+1/2}, \phi_{k+1/2})$, $q_\phi(i, j, k)$ at $(\theta_{i+1/2}, r_{j+1/2}, \phi_k)$ and the pressure at the cell centre $(\theta_{i+1/2}, r_{j+1/2}, \phi_{k+1/2})$. This implies that only the variable q_r has N_j values in the radial direction while it has $N_i - 1$ and $N_k - 1$ values in the longitude and colatitude directions, respectively. Similar considerations apply to the other velocity components.

Within the staggered discretization only q_r is located at the sphere origin $r_1 = 0$ (Fig. 2a) where, however, Equation (4b) does not need to be solved because $q_r(i, 1, k) \equiv 0$ is a boundary condition.

The same argument applies to Equation (4c) in which, for $\phi = 0$ and $\phi = \pi$, it results $q_\phi \equiv 0$.

The variable change combined with the staggered discretization allows the straightforward computation of *almost* all terms of Equations (3, 4a–4c) without coping with the singularities. As an example, we take the term $(1/r^2)\partial(q_r q_\phi)/\partial r$ of the q_ϕ equation for which, because of the staggering, the first radial node is at $j = 3/2$. Evidencing by bold face the indices in the differentiated direction we obtain:

$$\frac{1}{r^2} \frac{\partial q_r q_\phi}{\partial r} \Big|_{i+\frac{1}{2}, \frac{3}{2}, k} \approx \frac{(q_r q_\phi)_{i+\frac{1}{2}, \mathbf{2}, k} - (q_r q_\phi)_{i+\frac{1}{2}, \mathbf{1}, k}}{r_{\frac{3}{2}}^2 (r_{\mathbf{2}} - r_{\mathbf{1}})}. \quad (5)$$

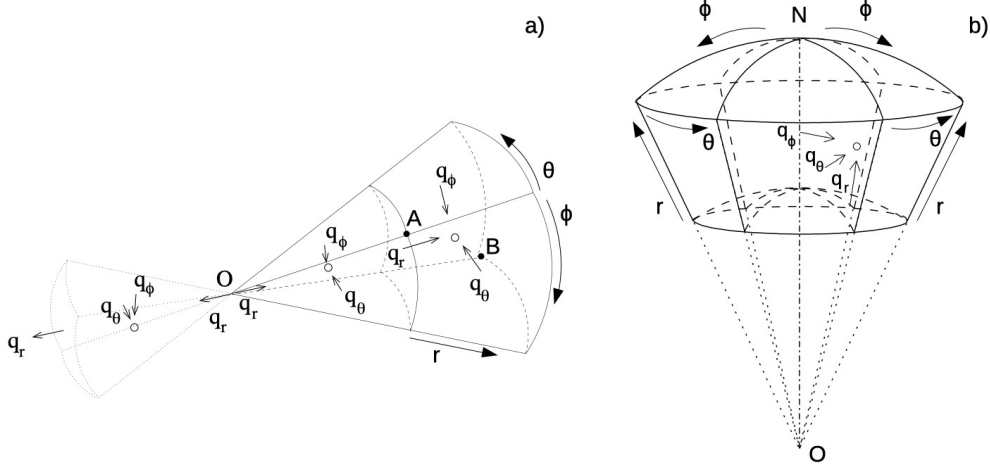


Figure 2: a) Staggered arrangement of the discrete variables and cells next to the sphere centre. b) Cells near the North pole of the sphere.

While we have omitted all the averages needed to locate the unknowns at the appropriate positions for the differentiation, (e.g. $(q_r q_\phi)_{i+1/2,2,k} = [q_r(i, 2, k+1) + q_r(i, 2, k)][q_\phi(i, 3, k) + q_\phi(i, 2, k)]/4$) we note that all the quantities are perfectly defined ($r_{3/2} = \Delta r_1/2$ and $(q_r)_{i+1/2,1,k} = 0$) and the derivative can be computed without any problem.

Along the same line, the term $1/(r \sin \phi) \partial(q_\theta q_\phi)/\partial \phi$ of the q_θ equation computed at the North pole ($k = 3/2$) node yields:

$$\left. \frac{1}{r \sin \phi} \frac{\partial q_\phi q_\theta}{\partial \phi} \right|_{i,j+\frac{1}{2},\frac{3}{2}} \approx \frac{(q_\theta q_\phi)_{i,j+\frac{1}{2},2} - (q_\theta q_\phi)_{i,j+\frac{1}{2},1}}{r_{j+\frac{1}{2}} \sin \phi_{\frac{3}{2}} (\phi_2 - \phi_1)}, \quad (6)$$

that, again, is not singular neither at the North pole ($\sin \phi_{3/2} \neq 0$) nor at the first radial node ($r_{3/2} \neq 0$).

The evaluation of the viscous terms at the origin ($r = 0$) and at the poles ($\phi = 0$ and $\phi = \pi$) benefits from the presence of the metrics that avoid the explicit computation of derivatives at these locations. For example, the discrete term $(1/r^2) \partial/\partial r (r^2 \partial q_\theta / \partial r)$ in the q_θ equation at $j = 3/2$ is:

$$\left. \frac{1}{r^2} \frac{\partial}{\partial r} r^2 \frac{\partial q_\theta}{\partial r} \right|_{i,\frac{3}{2},k+\frac{1}{2}} \approx \quad (7)$$

$$\frac{1}{r_2^{\frac{3}{2}}} \left[\left(r^2 \frac{\partial q_\theta}{\partial r} \right)_{i,2,k+\frac{1}{2}} - \left(r^2 \frac{\partial q_\theta}{\partial r} \right)_{i,1,k+\frac{1}{2}} \right] / (r_2 - r_1),$$

that does not need the evaluation of $\partial q_\theta / \partial r$ at $j = 1$ being multiplied by $r_1 \equiv 0$.

Similarly, the term $1/(r^2 \sin \phi) \partial / \partial \phi (\sin \phi \partial q_r / \partial \phi)$ of the q_r equation at the North pole reads:

$$\frac{1}{r^2 \sin \phi} \frac{\partial}{\partial \phi} \sin \phi \frac{\partial q_r}{\partial \phi} \Big|_{i+\frac{1}{2},j,\frac{3}{2}} \approx \quad (8)$$

$$\frac{1}{r_j^2 \sin \phi_{\frac{3}{2}}} \left[\left(\sin \phi \frac{\partial q_r}{\partial \phi} \right)_{i+\frac{1}{2},j,2} - \left(\sin \phi \frac{\partial q_r}{\partial \phi} \right)_{i+\frac{1}{2},j,1} \right] / (\phi_2 - \phi_1)$$

and it does not need the evaluation of $\partial q_r / \partial \phi$ at $k = 1$ since $\sin \phi_1 \equiv 0$. Note that the term $1/r^2$ is not a problem because the q_r equation is evaluated only for $j \geq 2$.

Despite the change of variables and the staggered discretization still there are few terms that need a special treatment at the singular points; one of them is $\partial / \partial r [r^2 \partial (q_r / r^2) / \partial r]$ of the q_r equation that for $j = 2$ becomes

$$\begin{aligned} \frac{\partial}{\partial r} r^2 \frac{\partial q_r / r^2}{\partial r} \Big|_{i+\frac{1}{2},2,k+\frac{1}{2}} &\approx \left\{ r_{\frac{5}{2}}^2 \left[\frac{(q_r)_{i+\frac{1}{2},3,k+\frac{1}{2}}}{r_3^2} - \frac{(q_r)_{i+\frac{1}{2},2,k+\frac{1}{2}}}{r_2^2} \right] / (r_3 - r_2) \right. \\ &\quad \left. - r_{\frac{3}{2}}^2 \left[\frac{(q_r)_{i+\frac{1}{2},2,k+\frac{1}{2}}}{r_2^2} - \frac{(q_r)_{i+\frac{1}{2},1,k+\frac{1}{2}}}{r_1^2} \right] / (r_2 - r_1) \right\} / (r_{\frac{5}{2}} - r_{\frac{3}{2}}), \end{aligned} \quad (9)$$

with the quantity $(q_r)_{i+1/2,1,k+1/2}/r_1^2$ that can not be evaluated directly.

A possible strategy is to transform the derivative

$$\frac{\partial}{\partial r} r^2 \frac{\partial q_r / r^2}{\partial r} \equiv \frac{\partial^2 q_r}{\partial r^2} - \frac{\partial}{\partial r} \left(\frac{2q_r}{r} \right), \quad (10)$$

whose right hand side that can be computed in a straightforward way. It is worth mentioning, however, that the above equivalence is valid only in the continuum limit while differences arise when both sides are discretized.

A different approach is to maintain the formulation (9) and replace the singular quantity by a surrogate obtained by an average with the two counterparts ‘opposite’ to the singular point. This approach had already been

used successfully for the axis of polar cylindrical coordinates by [36] and [1] although it has to be modified in the spherical case since the singularities at the centre and at the polar axis need a different treatment.

In the case of Equation (9) we recall that $q_r/r^2 = u_r$ and use the second-order midpoint interpolation $u_r(\theta, 0, \phi) = (u_r(\theta, \Delta r, \phi) - u_r(\theta + \pi, \Delta r, \pi - \phi))/2 + \mathcal{O}(\Delta r^2)$ in which the minus comes from the opposite orientation of the radial velocity in the mirror plane (Fig. 2a). With the discrete variables we have

$$\frac{q_r(i, 1, k)}{r_1^2} \approx \frac{1}{2} \left[\frac{q_r(i, 2, k)}{r_2^2} - \frac{q_r(i + N_{ir}/2, 2, N_{kr} - k)}{r_2^2} \right], \quad (11)$$

with $N_{ir} = N_i - 1$ and $N_{kr} = N_k - 1$ the number of q_r points in the azimuthal and colatitude directions, that make possible the evaluation of the viscous term through (9).

All the other terms needing the evaluation at $j = 1$ of q_r/r^2 can be treated in the same way.

Similarly, for the q_ϕ equation, the term $(1/r)\partial(q_\phi q_\phi/\sin\phi)$ requires the evaluation of $q_\phi/\sin\phi$ at $k = 1$ and $k = N_k$ which can not be done directly. Again we use the relation $q_\phi/\sin\phi = u_\phi$ and write $u_\phi(\theta, r, 0) = (u_\phi(\theta, r, \Delta\phi) - u_\phi(\theta + \pi, r, \Delta\phi))/2 + \mathcal{O}(\Delta\phi^2)$ that with the discrete variables becomes:

$$\frac{q_\phi(i, j, 1)}{\sin\phi_1} \approx \frac{1}{2} \left[\frac{q_\phi(i, j, 2)}{\sin\phi_2} - \frac{q_\phi(i + N_{i\phi}/2, j, 2)}{\sin\phi_2} \right], \quad (12)$$

with $N_{i\phi} = N_1 - 1$ and a similar expression for $\phi = \pi$ ($k = N_k$). The same approach can be adopted for the viscous term needing the evaluation of $q_\phi/\sin\phi$ at the polar axis.

Note that, differently from the sphere centre, at the polar axis there is no colatitude inversion to select the mirror point.

A possible cause of concern is that the special discretizations of some singular terms couple the meridional plane at θ_i with that at $\theta_i + \pi$ thus creating communication issues which would impede performance on highly parallel computers. This is however not the case since the above procedures require only one extra halo cell at the singular point and the involved data communication is irrelevant. In fact the same strategy is used in [32] for the equations in cylindrical coordinates that are solved on massive parallel computers using up to 3.2×10^4 processors.

3. Numerical Method

Equations (3, 4a–4c) are integrated using the fractional–step method detailed in [1] and briefly summarized below. The momentum equation for $\mathbf{q} = (q_\theta, q_r, q_\phi)$ is provisionally advanced in time using the old pressure field:

$$\frac{\hat{\mathbf{q}} - \mathbf{q}^l}{\Delta t} = \left[\gamma^l \mathbf{N}^l + \rho^l \mathbf{N}^{l-1} - \alpha^l \nabla p^l + \alpha^l \frac{\hat{\mathbf{V}} - \mathbf{V}^l}{2} \right]. \quad (13)$$

Here the superscript l indicates the time–step level, α^l , γ^l and ρ^l are the coefficients of the time integration scheme (second–order Adams–Bashfort or third–order Runge–Kutta). \mathbf{N} contains the explicit nonlinear terms, body forces and the off–diagonal viscous terms, while \mathbf{V} the implicit diagonal viscous terms.

Since the pressure is not updated, the resulting velocity field is not locally free–divergent and is denoted by $\hat{\mathbf{q}}$. The correct velocity, however, must differ from the provisional one only by a gradient term, thus we can write:

$$\mathbf{q}^{l+1} = \hat{\mathbf{q}} - \alpha^l \Delta t \nabla \Phi, \quad (14)$$

whose divergence yields the elliptic equation for the unknown correction:

$$\nabla^2 \Phi = \frac{\nabla \cdot \hat{\mathbf{q}}}{\alpha^l \Delta t}. \quad (15)$$

Once the scalar field Φ is determined, the solenoidal velocity \mathbf{q}^{l+1} is computed by Equation (14) and the new pressure through:

$$p^{l+1} = p^l + \Phi - \frac{\alpha^l \Delta t}{2Re} \nabla^2 \Phi. \quad (16)$$

The implicit treatment of the diagonal viscous terms of (13) would require the inversion of a large sparse matrix that is very time consuming; this is avoided by using the approximate factorization technique of [37] that requires only the inversion of three tridiagonal matrices with an error $\mathcal{O}(\Delta t^3)$.

Being the nonlinear convective terms computed explicitly, the equations should satisfy only the $CFL = \max[|\Delta t(r \sin \phi \Delta \theta / u_\theta)| + |\Delta t(r / u_r)| + |\Delta t(r \Delta \phi / u_\phi)|]$ stability conditions that is $CFL \leq 1$ for the Adams–Bashfort and $CFL \leq \sqrt{3}$ for the third–order Runge–Kutta scheme. The off–diagonal viscous terms, however, are also computed explicitly to avoid the implicit coupling of the

three momentum equations and this deteriorates the stability properties of the scheme. The actual CFL value used for the simulations therefore must be reduced with respect to the theoretical value and the amount of reduction depends on the Reynolds number and on the specific flow. In our applications we have found that halving the convective CFL limit yields a safe enough condition that allows the stable integration of the equations; it is worth mentioning, however, that this criterion must be taken as a rule of thumb and not as a strict limitation.

The current implementation of the method allows the use of generic non-uniform mesh distributions in the radial and colatitude directions. The reason for maintaining the uniform discretization in the remaining longitudinal direction is that we use trigonometric expansions and fast-Fourier-transforms to reduce the elliptic Equation (15) to a series of two-dimensional Helmholtz equations in the other two coordinates that are solved using the direct method of [38] or [39].

4. Results

In this Section we assess the qualities of the proposed numerical method by showing several numerical examples and benchmarking them with the results from other codes or those available from the literature.

4.1. Hill vortex

As a first example we consider a spherical Hill vortex [40] which is an exact solution of the Euler equations and, in the inviscid limit, preserves its shape and propagates with a constant velocity along a rectilinear trajectory.

The vortex is defined by assigning its toroidal vorticity $\omega = A\sigma$ within the sphere of radius a and centre C with an irrotational flow outside; the translation velocity of the ring is then $U_0 = 2Aa^2/15$ (Fig. 3a) and the Reynolds number is defined as $Re = 2aU_0/\nu$. Different initial positions C and velocity orientations U_0 have been simulated in order to stress the stability, the accuracy and the reliability of the method.

If not specified otherwise, the simulations have been performed in a domain of radius $R = 7a$ discretized by a mesh of 129^3 nodes using $Re = 2500$.

In Fig. 3b we report the trajectory of the vortex, through the Cartesian coordinates of the velocity peak, that moves horizontally with a constant velocity and crosses the sphere centre ($r = 0$) (Fig. 4). It can be noted that while Y_C and Z_C remain negligible in time, X_C increases linearly thus

confirming the constant translation velocity. In fact, a close inspection of X_C reveals a small deviation with respect to the theoretical straight line; this is due to the finite viscosity of the flow ($Re = 2500$) that perturbs the exact inviscid solution and deforms the initial vortex shape. That the vortex deformation is indeed due to viscosity and not to the discretization on spherical coordinates is confirmed by the results of Fig. 5 in which the same Hill vortex has been evolved using the code in Cartesian coordinates AFiD [41]. From the same calculation we have extracted also the trajectory of the vortex that perfectly overlaps with its counterpart computed in spherical coordinates.

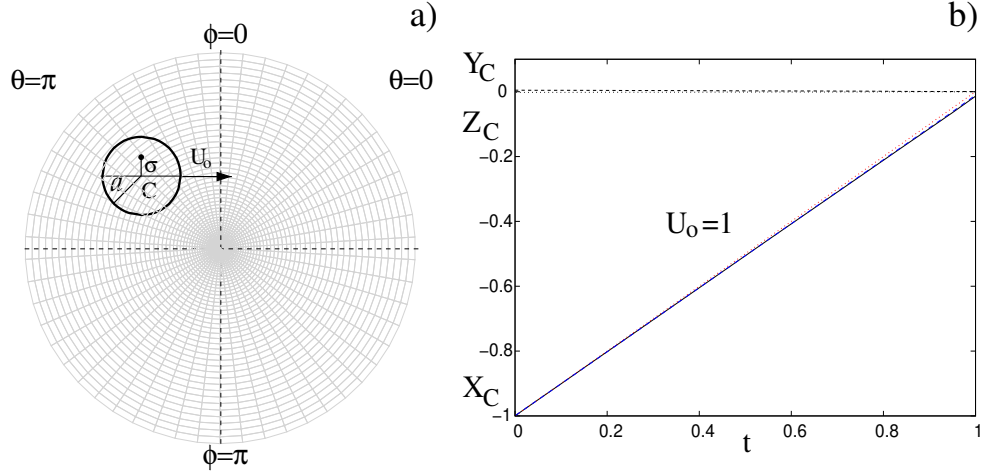


Figure 3: a) Sketch of the Hill vortex setup in the longitudinal sections $\theta = 0, \pi$ of the spherical domain. b) Time evolution of the vortex centre coordinates for the case at $Re = 2500$ with $\theta_C = \pi$, $r_C = 1$, $\phi_C = \pi/2$. — $X_C = r_C \cos \theta_C \sin \phi_C$, ---- X_C from the code in Cartesian coordinates [41], thin theoretical X_C ; ---- $Y_C = r_C \sin \theta_C \sin \phi_C$; — · — $Z_C = r_C \cos \phi_C$.

The same comparison between spherical and Cartesian codes has been repeated for a wide range of Reynolds numbers and in Fig. 6a we report the time evolution of the flow kinetic energy ($K = 0.5 \int_V \mathbf{u}^2 dV$), normalized by the initial value, for several Reynolds numbers showing that, despite the very different meshes, the kinetic energy decays always at an identical rate that depends only on Re .

Even if the results are the same, the simulations in spherical coordinates are more expensive than the Cartesian counterparts owing to the time step

limitations introduced by the mesh around $r = 0$. For example, using the third-order Runge–Kutta as time integration scheme and a working CFL of 1.2, the simulation at $Re = 2500$ on a 129^3 mesh in a 4^3 domain run with a time step $\Delta t \simeq 2 \times 10^{-2}$ throughout the whole computation. The same case on the spherical mesh had $CFL = 0.6$ with a dynamically adjusted time step of $\Delta t \simeq 10^{-2}$, when the vortex was far from the sphere centre, and $\Delta t \simeq 10^{-4}$ during the crossing phase. As a result, the CPU time for the latter simulation was about 14 times bigger than that of the former.

We wish to point out that the reason for this large computational overhead is the Hill vortex flow that, with its strongest velocity components perpendicular to the polar axis near the sphere centre, is particularly unsuitable for the spherical discretization. Nevertheless it has been chosen on purpose, in order to show that the numerical method can be used even in the most unfavourable conditions without losing stability or precision. It is important to note that the time step limitation is mainly given by the discretization at the sphere centre and not by the polar axis. In fact, later in this section we show that when the Hill vortex has an initial offset of $\phi_C = 2\pi/3$, with respect to the symmetry plane $\phi = \pi/2$, the time step reduction during the crossing of the polar axis is only a factor ≈ 3 –4 even if the largest velocity is still perpendicular to the coordinate line $\phi = 0$. Finally, in the next sections we will consider numerical examples in which the flow evolves in between two spherical shells and there the time step is limited only by the radial refinement of the mesh at the solid boundaries and not by the singularity at the polar axis.

Since the most critical phase of the simulation is the vortex centre crossing the point $r = 0$, here we have evaluated the code accuracy by assuming as reference solution that performed on the finest mesh $1459 \times 1297 \times 730$ (in θ , r and ϕ) and comparing it with grids successively coarsened by a factor 3 in each direction. This coarsening factor is such that, on a staggered mesh, it allows to compare the velocity components of different grids without interpolation and therefore to compute the raw accuracy of the numerical method. This set of simulations has been run with the same constant time step ($\Delta t = 6 \times 10^{-6}$) that was imposed by the stability of the simulation run on the finest mesh.

In Fig. 6b we report the L_2 -norm of the error computed for four meshes and, apart for the coarsest ($19 \times 17 \times 10$), the error decreases quadratically with the mesh size thus confirming the second-order accuracy.

We have further stressed the numerical method by giving the Hill vortex

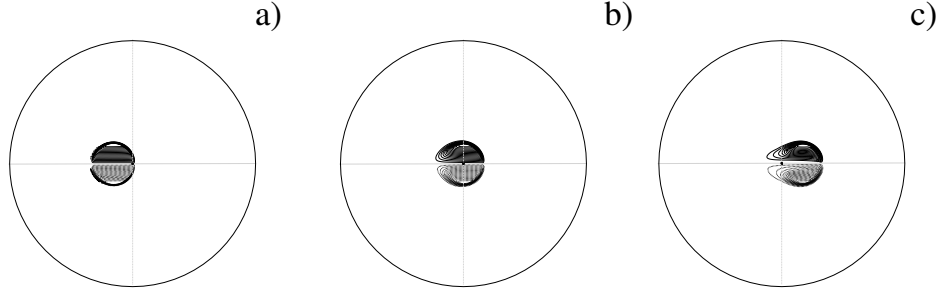


Figure 4: Time evolution of the Hill vortex at $Re = 2500$ in the longitudinal sections $\theta = 0, \pi$; longitudinal vorticity ($\Delta\omega_\theta = \pm 0.4$) for negative values; a)) $t = 0.5$, b) $t = 1.$, c) $t = 1.5$. Initial centre of the vortex: $\theta_C = \pi$, $r_C = 1$, $\phi_C = \pi/2$. Hereinafter, the black bullet indicates the origin of the spherical system.

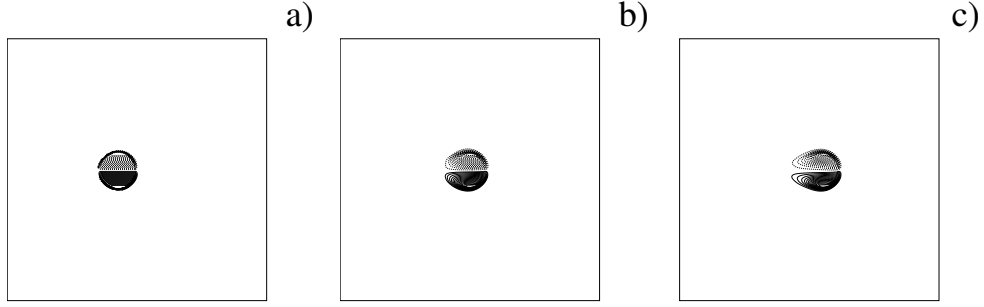


Figure 5: Time evolution of the Hill vortex at $Re = 2500$ evolved on a Cartesian uniform mesh; out-of-the-page vorticity ($\Delta\omega = \pm 0.4$) for negative values; a)) $t = 0.5$, b) $t = 1.$, c) $t = 1.5$.

an initial offset with respect to the symmetry plane $\phi = \pi/2$. It can be observed from Fig. 7 that in this case no coordinate lines are aligned with the vortex axis and nevertheless the vortex translates along a horizontal rectilinear trajectory showing the same dynamics as in Fig. 4. Also the total kinetic energy of the flow decays in time in the same way as the other $Re = 2500$ cases (Fig. 6a) and this confirms that the vortex evolution does not depend on the mesh orientation. Similarly to the case of Fig. 4, also for this simulation the time step has been dynamically computed in time

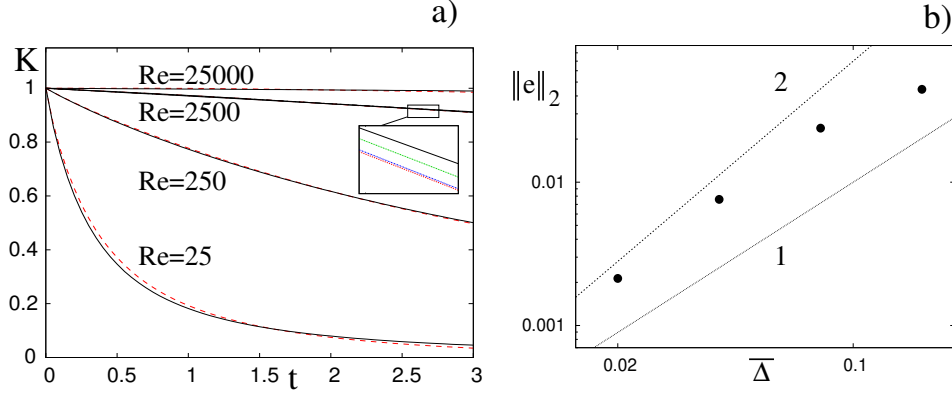


Figure 6: a) Decay of the total kinetic energy in time for the Hill vortex: — results from the code in spherical coordinates --- results from the Cartesian code [41]. In the inset: --- and $Re = 2500$ for the Hill vortex with initial offset. --- and $Re = 2500$ for the Hill vortex resolved on a mesh refined around the singular points. b) L_2 -norm of the error as function of the mesh size for the case at $Re = 2500$. ---- 2-slope, 1-slope. $\bar{\Delta}$ is the mean grid spacing defined as $\bar{\Delta} \equiv [V/(N_i N_j N_k)]^{1/3}$ with V the volume of the computational domain. $\theta_C = \pi$, $r_C = 1$, $\phi_C = \pi/2$.

to keep the CFL constant at the value of 0.6. In this case, however, it resulted $\Delta t \simeq 10^{-2}$ at the beginning of the simulation and it decreased to $\Delta t \simeq 2.7 \times 10^{-3}$ during the crossing of the polar axis. Considering that for a Hill vortex the largest velocity occurs at the centre, comparing Figs. 4b and 7b, it is clear that the most important limitation to the time step comes from the singularity around the sphere centre and not by that at the polar axis.

In another test we have positioned the vortex as in the case of Fig. 4 but the mesh has been refined at the sphere centre and at the polar axis (in both cases using a hyperbolic tangent distribution with stretching parameter 1.5) in order to exacerbate the stability problems of the integration in spherical coordinates. The results of Fig. 8a show that also in this case the vortex crosses the singular region without being distorted and the maximum divergence of the flowfield remains at machine precision throughout all the evolution (Fig. 8b). Also the total kinetic energy decay is identical to those of the other $Re = 2500$ cases (Fig. 6a) again showing a vortex dynamics independent of the mesh distribution.

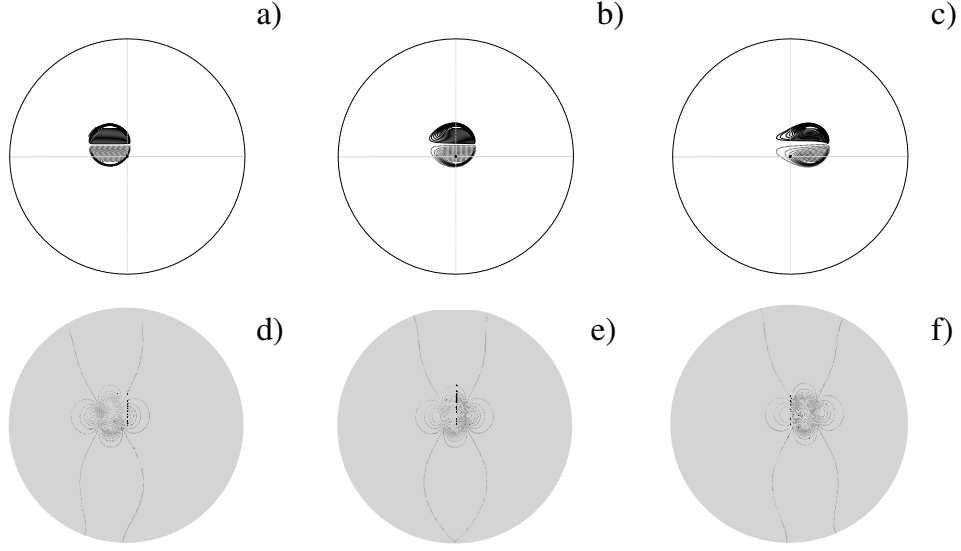


Figure 7: Time evolution of the Hill vortex at $Re = 2500$ in the longitudinal sections $\theta = 0, \pi$; top panels show longitudinal vorticity ($\Delta\omega_\theta = \pm 0.4$) for negative values; ($\Delta u = 0.1$) bottom panels for pressure ($\Delta p = 0.02$); the background mesh is shown with light gray lines. a) and d) $t = 0.5$, b) and e) $t = 1.$, c) and f) $t = 1.5$. Initial centre of the vortex: $\theta_C = \pi$, $r_C = 1$, $\phi_C = 2\pi/3$.

4.2. Flow in a precessing and spinning sphere

[42] validated their pseudo-spectral method by replicating the same problem as in [19] who studied the flow in a precessing and spinning sphere. We benchmark our code using the same test case and, referring to the sketch of Fig. 1, we consider flow inside a sphere of radius R spinning about the x -axis at constant angular velocity Ω_s . The system has an additional precession angular velocity Ω_p about the z -axis and the sphere surface ($r = R$) is no-slip. Assuming R and $\Omega_s R$, respectively, as scaling length and velocity, the flow depends on two nondimensional parameters $Re = \Omega_s R^2 / \nu$ and $\Gamma = \Omega_p / \Omega_s$.

Following [19], [42] we solve the equations in the precessing reference frame

$$\frac{\partial \mathbf{u}}{\partial t} + \nabla \cdot (\mathbf{u}\mathbf{u}) = -\nabla P - 2\Gamma \hat{k} \wedge \mathbf{u} + \frac{1}{Re} \nabla^2 \mathbf{u}, \quad \nabla \cdot \mathbf{u} = 0, \quad (17)$$

being \hat{k} the unit vector of the z -axis and $P = p - (\Gamma^2/2)(\hat{k} \wedge \mathbf{r})^2$ the reduced pressure. The boundary condition for the nondimensional velocity at the

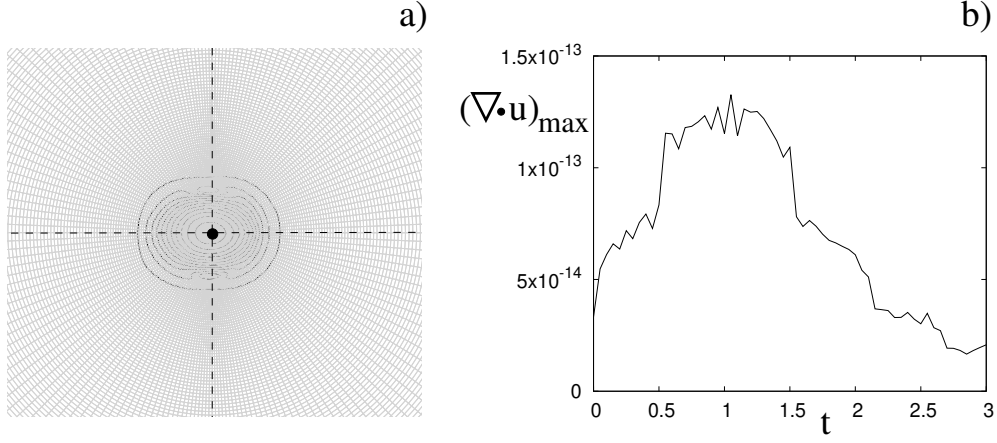


Figure 8: a) Zoom of velocity magnitude ($\Delta u = 0.1$) of a Hill vortex at $Re = 2500$ and $t = 1$ in the longitudinal sections $\theta = 0, \pi$; the computational mesh is refined on purpose around the singular points. b) Time evolution of the maximum divergence of the velocity field. Initial centre of the vortex: $\theta_C = \pi$, $r_C = 1$, $\phi_C = \pi/2$.

sphere surface is $\mathbf{u}|_{r=R} = \hat{x} \wedge \hat{r}$ with \hat{x} and \hat{r} the unit vectors of the x -axis and of the radius \mathbf{r} .

[19] analysed the flow for $\Gamma = 0.1$ and $Re \leq 500$ finding that a steady state is eventually achieved with increasingly entangled toroidal structures developed within the sphere. On the other hand, [42] observed that the flow structure could be better understood by plotting the velocity field in a reference frame rotating with the spinning sphere $\mathbf{v} = \mathbf{u} - \hat{x} \wedge \mathbf{r}$.

Here we consider the case at the highest Reynolds number $Re = 500$ and compare our results for the steady state solution of \mathbf{v} at the same three $z = \text{const}$ planes as reported by [42]. The simulations have been performed at the same resolution and the comparison, given in Fig. 9, shows excellent agreement.

Once again we note that in this numerical example, being the flow velocities very small at the sphere centre (see Figs. 9cf) the integration could be carried out at constant $CFL = 0.6$ with a nondimensional time step of $\approx 4 \times 10^{-2}$ and the limitation was generated by the fine mesh stretched at the sphere surface rather than from the singular points of the spherical coordinates.

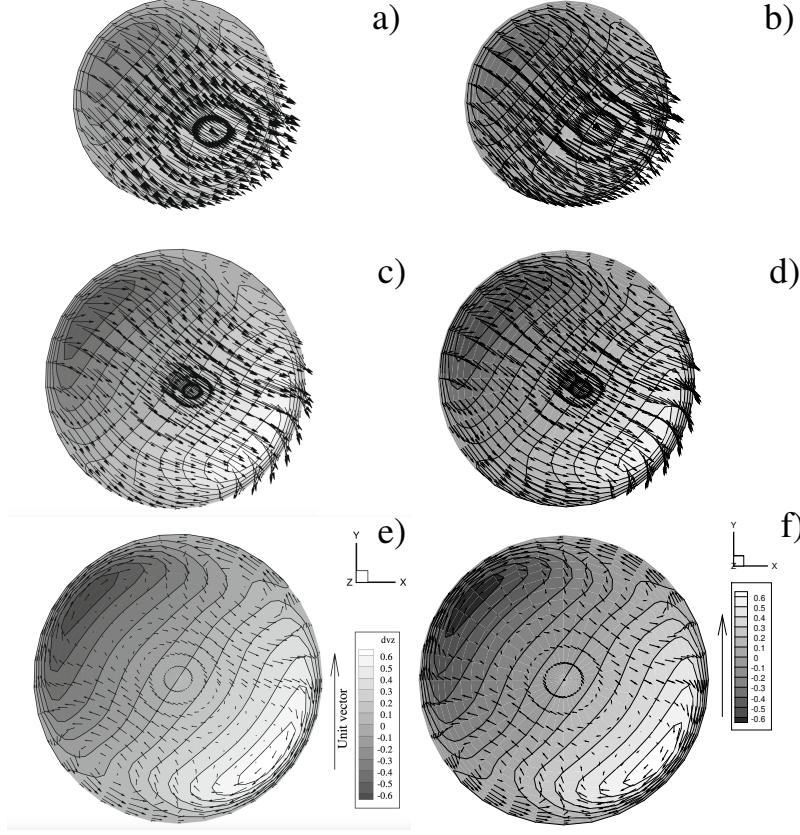


Figure 9: Flow in a precessing, spinning sphere at $\Gamma = 0.1$ and $Re = 500$. The velocity vectors of the field rotating with the spinning sphere \mathbf{v} are reported in the sections $z = -0.66$, a) and d); $z = -0.33$, b) and e); $z = 0$, c) and f). The contours are for the velocity component v_z . a), c) and e) are the results adapted from Fig. 7 of [42], b) ,d) and f), present results.

4.3. Rayleigh–Bénard convection with vertical gravity

In this example we consider the thermally driven flow developing between two concentric spheres of radii R_i and R_o whose surfaces are maintained at a temperature difference ΔT , the inner being hotter than the outer. Following the arrangement of [43] the gravity has a constant orientation and points vertically downward as in Fig. 10a.

The flow is solved using the Boussinesq approximation in which all the

fluid properties are independent of the temperature except for the density in the buoyancy term of the momentum equation. In addition to the conservation of mass and balance of momentum (Equations 2) here we need also the energy conservation that reduces to the convection–diffusion equation for the temperature field. The complete set of governing relations in non-dimensional vector form then reads:

$$\begin{aligned}\nabla \cdot \mathbf{u} &= 0, \\ \frac{\partial \mathbf{u}}{\partial t} + \mathbf{u} \cdot \nabla \mathbf{u} &= -\nabla p - \hat{g}T + \sqrt{\frac{Pr}{Ra}} \nabla^2 \mathbf{u}, \\ \frac{\partial T}{\partial t} + \mathbf{u} \cdot \nabla T &= \sqrt{\frac{1}{RaPr}} \nabla^2 T.\end{aligned}\tag{18}$$

$Ra = g\beta\Delta t(R_o - R_i)^3/(\nu\kappa)$ is the Rayleigh number with β the isobaric thermal expansion coefficient, κ the thermal diffusivity of the fluid, g the magnitude of the gravity and \hat{g} its unit vector; $Pr = \nu/\kappa$ is the Prandtl number. Referring to Equations (2) we can also write $\hat{g} = (f_\theta, f_r, f_\phi) = (\sin\theta, \sin\phi\cos\theta, \cos\phi\cos\theta)$.

Being the temperature a scalar quantity it is located at the cell centre (Fig. 2) and the solution of the last of Equations (18) in spherical coordinates does not present particular challenges at the singular points.

In the present flow, a buoyant plume is produced that ascends vertically thus the ‘natural’ arrangement is to have the gravity vector aligned with the polar axis so that there are no velocity vectors crossing it. In order to show that the proposed numerical method, performs well also in supposedly unfavourable conditions, we have repeated the simulation also with the gravity perpendicular to the polar axis.

In Fig. 10 we report the results for a case at $\eta = R_i/R_o = 0.5$, $Ra = 10^5$ and $Pr = 0.7$ that, after an initial transient, attains a steady state.

A usual way to express the heat transfer in thermally driven flows is by the Nusselt number defined as the ratio between the heat flux through a surface and its counterpart in absence of flow motion. For this problem it can be computed for the inner and the outer spheres to obtain:

$$Nu_o = -\frac{1}{\eta} \frac{\overline{\partial T}}{\partial r} \Big|_{r=R_i}, \quad Nu_i = -\eta \frac{\overline{\partial T}}{\partial r} \Big|_{r=R_o}, \tag{19}$$

where the $\overline{}$ indicates surface and time averages: if the flow is steady or it attains a statistical steady state the two values have to match.

Fig. 10b shows the time evolution of the inner and outer Nusselt numbers for the simulations with the gravity in two perpendicular orientations; it can be observed that not only they converge exactly to the same value but also the transient evolutions are indistinguishable. The asymptotic Nusselt number is $Nu = 3.4105$ in excellent agreement with the values $Nu = 3.4012$ of [43], 3.4890 of [44] 3.4648 of [45] and 3.3555 of [46].

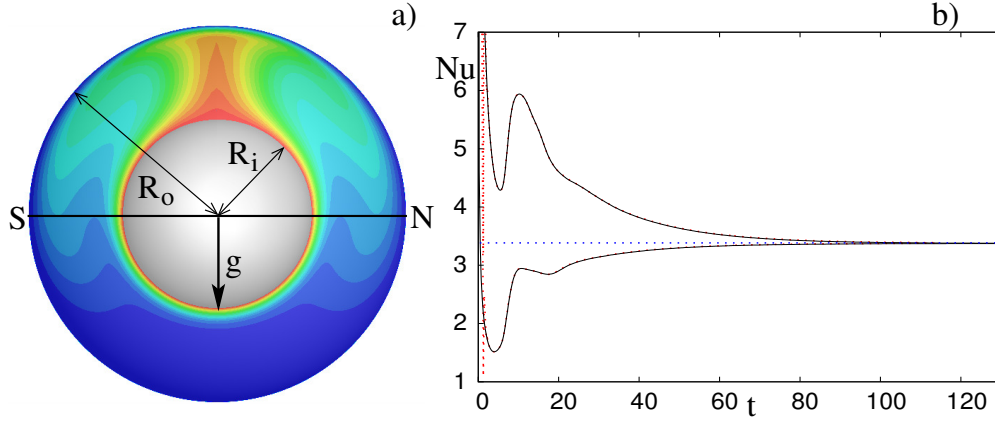


Figure 10: a) Section through the meridional planes $\theta = 0, \pi$ of temperature contours ($\Delta T = 0.1$) for the flow at $\eta = R_i/R_o = 0.5$, $Ra = 10^5$ and $Pr = 0.7$. Grid $65 \times 49 \times 49$. b) Time evolution of the Nusselt numbers — simulation with the gravity aligned with the polar axis, --- gravity perpendicular to the polar axis, reference value of $Nu = 3.4012$ from [43].

Another interesting result is that in both cases, with the gravity aligned or perpendicular to the polar axis, the simulation run at constant $CFL = 1$ yielded a time averaged nondimensional time step $\Delta t \approx 10^{-2}$ thus further confirming that the present numerical method alleviates the time step restrictions induced by the singularity at the poles.

4.4. Rayleigh–Bénard convection with central gravity

In this numerical example we use the same configuration as in the previous section except for the gravity that now points towards the centre of the sphere.

We rely again on Equations (18) with the non-dimensional gravity vector that now reads $\mathbf{g} = (f_\theta, f_r, f_\phi) = (0, g'(r), 0)$ with $g'(r) = (R_o/r)^2$ the non-dimensional radial distribution of gravity. The reason for choosing this

specific radial dependence is that, as shown by [48], in this case it is possible to derive exact relations among the Nusselt number and the dissipations:

$$Nu = \frac{Pr^2}{Ra} \frac{1 + \eta + \eta^2}{3} \epsilon_u + 1 = \frac{1 + \eta + \eta^2}{3\eta} \epsilon_T, \quad (20)$$

with $\epsilon_u = \langle (\nabla \times \mathbf{u})^2 \rangle$ the kinetic energy- and $\epsilon_T = \langle (\nabla T)^2 \rangle$ the temperature variance-dissipation rates averaged over the fluid volume and in time, that can be used to verify both, the consistency of the numerical method and to assess the statistical convergence of the results. In Fig. 11 we report the results for the case at $\eta = R_i/R_o = 0.6$, $Ra = 3 \times 10^4$ and $Pr = 1$. computed on a $129 \times 97 \times 97$ mesh. It can be observed that, after the initial transient ($t \leq 100$) the Nusselt numbers computed from Equations (19) and (20) oscillate around a common mean value and the simulation is stopped when their averages agree within 1%.

In addition to the heat transfer also the strength of the flow is used to quantify the response of the system and, in non-dimensional form, it can be expressed by the Reynolds number. In [48] it was measured by computing the root mean square of the velocity field that, however, was scaled by the viscous velocity scale $\nu/(R_o - R_i)$. Since in Equations (18) we have used the convective velocity $\sqrt{g\beta\Delta T(R_o - R_i)}$, the root mean square Reynolds number Re' of [48] corresponds to the quantity $\sqrt{2KRa/(VPr)}$ with V the fluid volume and K the kinetic energy of the flow already defined in section 4.1.

In Table 1 we report the values of Nu and Re' for some cases that show excellent agreement with the analogous values obtained by [48]. In the sake of conciseness we have not presented the Nusselt numbers obtained by the dissipations from the expressions (20) that, however, deviate from those computed by the wall temperature gradients always by less than 1% for every simulation.

Cases #5–#7 are grid refinements of the same flow: it is worthwhile to note that Case #5 has a mesh that is coarser than Case #6 only in the radial direction and the results are still correct. For the radial distribution of the computational nodes of case #5 we have observed from Equations (19) that being $Nu_i = Nu_o$ the temperature gradient at the inner sphere must exceed that at the outer sphere by a factor $1/\eta^2$. This implies that the wall resolution at the outer sphere can be coarser than that at the inner sphere and for the case at $\eta = 0.6$, $Pr = 1$ and $Ra = 3.0 \times 10^4$ this resulted

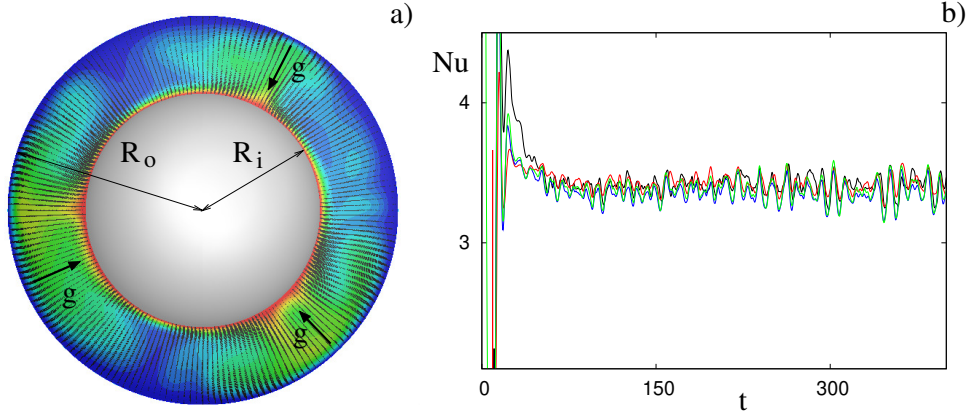


Figure 11: a) Section through the meridional planes $\theta = 0, \pi$ of temperature contours ($\Delta T = 0.1$) overlaid with velocity vectors for the flow at $\eta = R_i/R_o = 0.6$, $Ra = 3 \times 10^4$ and $Pr = 1..$ Grid $129 \times 97 \times 97$. b) Time evolution of the Nusselt numbers: — value computed at the inner surface, — value computed at the outer surface, — value computed from ϵ_u , — value computed from ϵ_T .

in a saving of about 25% of nodes. In this case, in particular, the radial distribution of the nodes has been assigned as an input from an external file built by third-order splines with the conditions $\Delta r = (R_o - R_i)/450$ at the inner sphere, $\Delta r = (R_o - R_i)/200$ at the outer sphere and $\Delta r = (R_o - R_i)/45$ halfway between the boundaries.

For these simulations, run only for validation purposes, this is not a crucial advantage since they can be run anyway within a few hours on a single Intel I7-2.7GHz processor. However, when the method is employed to tackle higher Rayleigh number flows implying meshes with hundreds of million ([48]) or billions ([32]) of nodes the asymmetric radial stretching of the mesh could become very attractive and this is possible thanks to the flexibility of the finite-difference schemes.

4.5. Space-developing jet

In this last application we simulate the spatial evolution of a round jet of initial diameter d and mean inflow velocity U_{in} with a Reynolds number $Re = U_{in}d/\nu$. Here we follow the idea of [31] who noted that the coordinate lines of a spherical shell sector naturally follow the self-similar spreading of a jet. Another advantage is that the divergence of the θ - and ϕ -isolines yield a more refined mesh for small radii while it coarsens as the radius increases.

Case	Ra	Nu	Re'	$N_\theta \times N_r \times N_\phi$	Nu [48]	Re' [48]
1	1.5×10^3	1.327	4.37	$65 \times 33 \times 49$	1.33	4.4
2	3.0×10^3	1.812	9.70	$65 \times 33 \times 49$	1.80	9.6
3	1.0×10^4	2.527	23.43	$65 \times 33 \times 49$	2.51	23.3
4	1.5×10^4	2.828	29.83	$97 \times 65 \times 65$	2.81	29.8
5	3.0×10^4	3.428	43.95	$97 \times 49 \times 65$	3.40	44.0
6	3.0×10^4	3.443	43.94	$97 \times 65 \times 65$	3.40	44.0
7	3.0×10^4	3.412	43.97	$129 \times 97 \times 97$	3.40	44.0
8	5.0×10^4	3.924	57.24	$97 \times 65 \times 65$	3.89	57.5

Table 1: Main input and out parameters and comparison with the results from [48]. All the simulations are run at $\eta = 0.6$ and $Pr = 1$.

The computational domain, reported in Fig. 12a, is defined as $0 = \Theta_i \leq \theta \leq \Theta_f = \pi/6$, $R_i = 3 \leq r \leq 12 = R_o$, and $11\pi/12 = \Phi_i \leq \phi \leq \Phi_f = 13\pi/12$ and, since it does not contain any of the singular points, the solution of the governing equations is performed easily. In fact, the reason for performing this last test case has not to do with the equation singularity but rather with the possibility of the scheme to deal with ‘complex’ boundary conditions.

At the inner boundary ($r = R_i$) a radial velocity profile with mean U_{in} is prescribed within the circle of diameter d and centre $([\Theta_i + \Theta_f]/2, [\Phi_i + \Phi_f]/2)$ and perturbed with a white noise of amplitude $0.02U_{in}$. At the outflow we impose the convective boundary condition as in [49]:

$$\frac{\partial q_i}{\partial t} + U_R \frac{\partial q_i}{\partial r} = 0, \quad (21)$$

that advects all the velocity components q_i out of the domain with the velocity U_R that is dynamically adjusted to assure mass conservation to the machine precision. Periodicity is imposed in the azimuthal and colatitude directions.

The simulation has been performed on a mesh of $97 \times 257 \times 97$ nodes at a Reynolds number $Re = 5000$ and an instantaneous snapshot of the velocity magnitude through the mean plane $\theta = (\Theta_i + \Theta_f)/2$ is shown in Fig. 12b.

We wish to point out that our azimuthal and colatitude periodic boundaries are different from those of [31] who used traction-free conditions [50] at these lateral planes. The latter (obtained by imposing the scalar product between the total stress tensor and the boundary normal to be zero) are

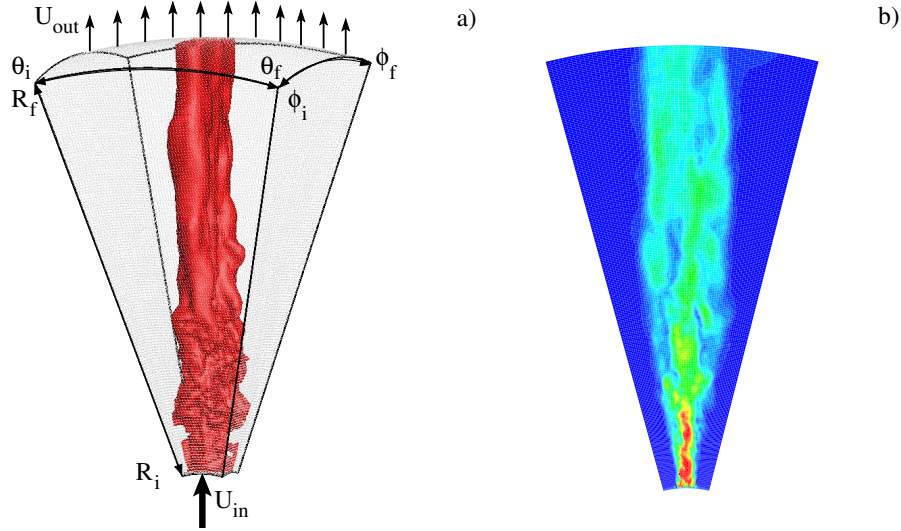


Figure 12: a) Computational set-up for the space developing jet. The isosurface is velocity magnitude $|\mathbf{u}| = 0.2$. b) Instantaneous snapshot plane section ($\theta = (\theta_i + \theta_f)/2$) of velocity magnitude (from blue to red) $\Delta |\mathbf{u}| = 0.1$.

certainly more correct since they allow flow transpiration without yielding stress in contrast to periodicity that, representing an infinite array of jets, unavoidably induces some confinement. Owing to this important difference, we do not make any quantitative claim about the dynamics of the jet and do not attempt comparisons with [31]; we use this calculation only to show the flexibility of the proposed method that allows within the same ease the imposition of simple, homogeneous boundary conditions, such as the no-slip of sections 4.3 and 4.4, and the inhomogeneous inflow/outflow conditions of the space-developing jet.

5. Conclusions

In this paper we have shown that the combination of a change of variables with a central-, second-order accurate finite-differences on a staggered mesh and the special treatment of some discrete terms removes the singularities of the Navier-Stokes equations for an incompressible viscous flow in spherical coordinates.

Some numerical applications have been considered with the aim of stress-

ing the stability of the scheme and its capability to reproduce reference results.

Most of the tests have been performed using a spherical Hill vortex that, in the inviscid limit, is an exact solution of the governing equations and propagates along a rectilinear trajectory with a constant velocity. The numerical procedure has shown to be second-order accurate and to reproduce the results obtained for the same flows by a code in Cartesian coordinates. The method performed equally well even when the vortex centre was offset with respect to the symmetry plane $\phi = \pi/2$ or the mesh was unnecessarily refined around the singular points.

Another benchmark has been performed by simulating the flow within a precessing, spinning sphere for the same parameters as those considered by [19] and [42] obtaining a perfect agreement with their results produced by spectral methods.

Equally good results have been obtained for thermally driven flows in which only the singularity at the polar axis was present although the flow physics was enriched by the presence of the additional temperature field; the heat transfer of these flows was always in excellent agreement with other similar studies and even the exact relations between heat transfer and dissipation rates were perfectly satisfied.

An important drawback related to the spherical coordinates is the time step limitation introduced by the discretization around the singularities. The proposed numerical method has shown to alleviate this problem for the polar axis and, for the flow in spherical shells with the grid stretched radially at the solid boundaries, the restriction induced by the latter outweighs that of the former. On the other hand, the singularity at the sphere centre still introduces strong time step limitations, although only if the largest flow velocity occurs there.

Although the merits of the proposed numerical method have been evidenced by reproducing simple canonical flows, for which benchmark results are available, its main merits are related to the flexibility of finite-differences. In the evolution of a space developing round jet (Section 4.5) we have qualitatively shown the possibility to use complex inflow/outflow boundary conditions while for the thermal convection with central gravity we have employed generic nonuniform meshes (Case # 5 of Section 4.4).

These finite-difference features are particularly appealing if the code has to be applied to realistic flows, such as the mantle convection of a planet [51], in which complex boundary conditions, but also inhomogeneous forcings and

variable fluid properties, have to be accounted for.

Another important advantage of finite-difference methods is the relative ease of parallelization related to the local nature of the discrete differencing; this is true also for the present scheme inspired by that of [1] and with the same variable arrangement and memory layout. The latter has been massively parallelized in [32] and run on up to 3.2×10^4 cores. Also the present scheme in spherical coordinates has been parallelized and it is already running on hundreds of processors to simulate thermally driven turbulent flows; these results will be the subject of a forthcoming paper.

References

- [1] Verzicco, R. & Orlandi, P., 1996, A Finite-Difference Scheme for Three-Dimensional Incompressible Flows in Cylindrical Coordinates, *J. of Comp. Phys.*, **123**, 402–414.
- [2] Rolf, T. & Tackley, J.P., 2001, Focussing of stress by continents in 3D spherical mantle convection with self-consistent plate tectonics *Geophys. Res. Lett.*, **38**, L18301.
- [3] Constantin, A. & Johnson, R.S., 2018, Steady large-scale ocean flows in spherical coordinates. *Oceanography*, **31**(3), 42–50.
- [4] , Randall, D. A., Ringler, T. D., Heikes, R. P., Jones, P., & Baumgardner, J., 2002, Climate modeling with spherical geodesic grids. *Computing in Science & Engineering*, **4**(5), 32–41.
- [5] Aksenov, A.G., Babakov, A.V. & Chechetkin, V.M., 2018, Mathematical Simulation of Vortex Structures in Rapidly Rotating Astrophysical Objects. *Comput. Math. and Math. Phys.*, **58**, 1287–1293.
- [6] Glatzmaier, G., 1984, Numerical simulations of stellar convective dynamos. I. The model and method, *J. of Comp. Phys.*, **55**, 461–484.
- [7] Kissmann, R, Kleimann, J., Krebl, B. & Wiengarten, T., 2018, The CRONOS Code for Astrophysical Magnetohydrodynamics, *The Astrophys. J. Supp. Series*, **236**(53), 26pp.
- [8] Oschmann, T. & Kruggel-Emden, H., 2018, A novel method for the calculation of particle heat conduction and resolved 3D wall heat transfer for the CFD/DEM approach *Powder Tech.*, **338**, 289–303.

- [9] Busse, F.H., 1975, Patterns of convection in spherical shells. *J. Fluid Mech.*, **72**, 67–85.
- [10] Kida, S., 1994 Stability of Thermal Convection in a Rapidly Rotating Sphere, *J. of Phys. Soc. Jap.*, **63**(8), 2964–2973.
- [11] Seyboldt, R & Jülicher, F., 2018, Role of hydrodynamic flows in chemically driven droplet division *New J. of Phys.*, **20**, 105010.
- [12] Bodenheimer, P., Laughlin, G.P., Rózycka, M. & Yorke, H.W., 2007, Numerical Methods for Astrophysics. An Introduction, Taylor & Francis, NY, 352 pp.
- [13] Orlandi, P. & Verzicco, R., 1993, Vortex rings impinging on walls: axisymmetric and three-dimensional simulations, *J. Fluid Mech.*, **256**, 615–656.
- [14] Shariff, K., Verzicco, R. & Orlandi, P., 1994, A numerical study of three-dimensional vortex ring instabilities: viscous corrections and early nonlinear stage, *J. Fluid Mech.*, **279**, 351–375.
- [15] Fornberg, B., 1995, A pseudospectral approach for polar and spherical geometries *SIAM J. Sci. Comput.*, **16**(5), 1071–1081.
- [16] Kitauchi, H., Araki, K. & Kida, S., 1997, Flow structure of thermal convection in a rotating spherical shell, *Nonlinearity*, **10**, 885–904.
- [17] Tilgner, A., 1999, Spectral methods for the simulation of incompressible flow in spherical shells, *Int. J. Num. Methods Fluids*, **30**, 713–724.
- [18] Kageyama, A. & Kida, S., 2000, A Spectral Method in Spherical Coordinates with Coordinate Singularity at the Origin, *Research Report*, **NIFS-636**.
- [19] Kida, S. & Nakayama, K., 2008, Helical Flow Structure in a Precessing Sphere, *J. of Phys. Soc. Jap.*, **77**(5), 054401.
- [20] Kida, S. & Shimizu, M., 2011, A turbulent ring and dynamo in a precessing sphere, *J. of Phys.*, **318**, 072031.

- [21] Auteri, F. & Quartapelle, L., 2009, NavierStokes spectral solver in a sphere, *J. of Comput. Phys.*, **228**, 7197–7214.
- [22] Moin, P. & Verzicco, R., 2016, On the suitability of second-order accurate discretizations for turbulent flow simulations, *Eur. J. Mech. B/Fluids*, **55**(2), 242–245.
- [23] Williams, G.P. & Robinson, J.B., 1973, Dynamics of a convectively unstable atmosphere: Jupiter? *J. of Atmos. Sci.*, **30**, 684–717.
- [24] Gilman, P.A., 1975, Linear simulations of Boussinesq convection in a deep rotating spherical shell, *J. of Atmos. Sci.*, **32**, 1331–1352.
- [25] Gilman, P.A., 1977, Nonlinear dynamics of boussinesq convection in a deep rotating spherical shell–I, *Geophys. Astrophis. Fluid Dynamics*, **8**, 93–135.
- [26] Cullen, M.J.P., 1983, Current Progress and Prospects in Numerical Techniques for Weather Prediction Models, *J. of Comp. Phys.*, **50**, 1–37.
- [27] Kageyama, A., Watanabe, K. & Sato, T., 1993, Simulation study of a magnetohydrodynamic dynamo: Convection in a rotating spherical shell, *Physics of Fluids B*, **5**, 2793–2805.
- [28] Aubert, J., Aurnou, J. & Wicht, J., 2008, The magnetic structure of convection–driven numerical dynamos, *Geophys. J. Int.*, **172**, 945–956.
- [29] Sha, W., Nakabayashi, K. & Ueda, H., 1998, An Accurate Second-Order Approximation Factorization Method for Time Dependent Incompressible Navier-Stokes Equations in Spherical Polar Coordinates, *J. Comp. Phys.*, **142**, 47–66.
- [30] Mohseni, K. & Colonius, T. 2000, Numerical Treatment of Polar Coordinate Singularities, *J. Comp. Phys.*, **157**, 787–795.
- [31] Boersma, B.J., Brethouwer, G. & Nieuwstadt, F.T.M., 1998, A numerical investigation on the effect of the inflow conditions on the self-similar region of a round jet, *Phys. of Fluids*, **10**(4), 899–909.

- [32] Stevens, R.J.A.M., Verzicco, R. & Lohse, D., 2010, Radial boundary layer structure and Nusselt number in RayleighBnard convection, *J. Fluid Mech.*, **643**, 495–507.
- [33] Batchelor, G.K., 1967, An introduction to Fluid Mechanics, Cambridge Univ. Press, 615 pp.
- [34] Rosenfeld, M., Kwak, D. & Vinokur, M., 1991, A Fractional Step Solution Method for the Unsteady Incompressible Navier–Stokes Equations in Generalized Coordinate Systems, *J. Comput. Phys.*, **94**, 102–137.
- [35] Harlow, F.H. & Welch, J.E., 1965, Numerical Calculation of Times–Dependent Viscous Incompressible Flow of Fluid with Free Surface, *Phys. of Fluids*, **8**, 2182–2189.
- [36] Eggels, J.C.M., Unger, F., Weiss, M.H., Westerweel, J., Adrian, R.J., Friedrich, R. & Nieuwstadt, F.T.M., 1994, Fully developed turbulent pipe flow: a comparison between direct numerical simulation and experiment, *J. Fluid Mech.*, **268**, 175–210.
- [37] Beam, R.M. & Warming, R.F., 1976, An implicit finite–difference algorithm for hyperbolic systems in conservation–law form, *J. Comput. Phys.*, **22**, 87–110.
- [38] Swarztrauber, P., 1974, A direct method for the discrete solution of separable elliptic equations, *SIAM J. Num. Analysis*, **11**, 1136–1150.
- [39] Lynch, R.E. & Rice, J.R. & Thomas, D.H., 1964, Tensor product analysis of partial difference equations, *Bull. Am. Math. Soc.*, **70**, 378–384.
- [40] Hill, M.J.M., 1894, VI. On a spherical vortex, *Phil. Trans. Roy. Soc. A*, **185**, 213–245.
- [41] van der Poel, E.P., Ostilla-Mónico, R., Donners, J., Verzicco, R., 2015, A pencil distributed finite difference code for strongly turbulent wall-bounded flows, *Computers & Fluids*, **116**, 10–16.
- [42] Autieri, F. & Quartapelle, L., 2009, NavierStokes spectral solver in a sphere, *J. Comput. Phys.*, **228**, 7197–7214.

- [43] Feldman, Y. & Colonius, T., 2013, On a transitional and turbulent natural convection in spherical shells, *Int. J. Heat Mass Transfer*, **64**, 514–525.
- [44] Chu, H. & Lee, T., 1993, Transient natural convection heat transfer between concentric spheres, *Int. J. Heat Mass Transfer*, **36**, 3159–3170.
- [45] Dehghan, A. & Masih, K., 2010, Numerical simulation of buoyancy-induced turbulent flow between two concentric isothermal spheres, *Heat Transfer Eng.*, **31**, 33–44.
- [46] , Chiu, C. & Chen, W., 1996, Transient natural convection heat transfer between concentric and vertically eccentric spheres, *Int. J. Heat Mass Transfer*, **39**, 1439–1452.
- [47] Wicht, J., 2002, Inner-core conductivity in numerical dynamo simulations, *Phys. of Earth and Plan. Int.*, **132**, 281–302.
- [48] Gastine, T., Wicht, J. & Aurnou, J.M., 2015, Turbulent Rayleigh–Bénard convection in spherical shells, *J. Fluid Mech.*, **778**, 721–764.
- [49] Salvetti, M.V., Orlandi, P. & Verzicco, R., 1995, Direct simulations of transitional axisymmetric coaxial jets. *AIAA J.*, **34**, 736–743.
- [50] Gresho, P.M., 1991, Incompressible fluid dynamics: Some fundamental formulations issues, *Annu. Rev. Fluid Mech.*, **23s**, 413–453.
- [51] Schubert, G., Turcotte, D.L. & Olson, P., 2004, Mantle Convection in the Earth and Planets, *Cambridge Univ. Press*, pp. 959.